Article

Unraveling 1-Hexene Hydrogenation over Dilute Pd-in-Au Alloys

Published as part of The Journal of Physical Chemistry virtual special issue "Cynthia Friend Festschrift".

Jessi E. S. van der Hoeven,* Hio Tong Ngan, George Yan, Joanna Aizenberg, Robert J. Madix, Philippe Sautet, and Cynthia M. Friend*

Read Online

ACCESS | Metrics & More | Article Recommendations | Supporting Information

ABSTRACT: Dilute Pd-in-Au alloys are valuable materials for selectively hydrogenating alkynes and isomerizing alkenes. By diluting Pd in a Au host, the selectivity toward semihydrogenated alkene isomers can be significantly enhanced and the unfavorable over-hydrogenation to alkanes is suppressed. However, a detailed mechanistic study on the origin of the enhanced alkene selectivity over dilute alloy catalysts is still missing. Here, we combine experiment and theory to unravel the reaction mechanism, identifying rate-limiting and selectivity-controlling steps in 1-hexene hydrogenation over dilute Pd-in-Au catalysts. Using isotope-exchange hydrogenation experiments, we show that 1-hexene and hydrogen over a bimetallic Pd_4Au_{96} in silica catalyst preferentially form 1-hexene isomers, (trans and cis) 2- and 3-hexene and only a small amounts of hexane. The reaction is consistent with a Horiuti−Polanyi mechanism, similar to a monometallic Pd nanoparticle catalyst. Computation of the free-energy profiles for 1-hexene hydrogenation and isomerization over a single Pd atom in a Au surface using first principles calculations indicated that the isomerization of 1-hexene to 2-hexene is energetically favorable due to the relatively large barrier for H_2 dissociation preventing hydrogenation to n-hexane. Microkinetic modeling established that H_2 dissociation on the single-atom Pd sites and H spillover from these sites onto the Au host are rate-limiting and key in steering the selectivity of dilute Pd-in-Au alloys toward the hexene isomers. The mechanistic insights from this study contribute to the rational design of optimized dilute alloy catalysts for selective alkene isomerization.
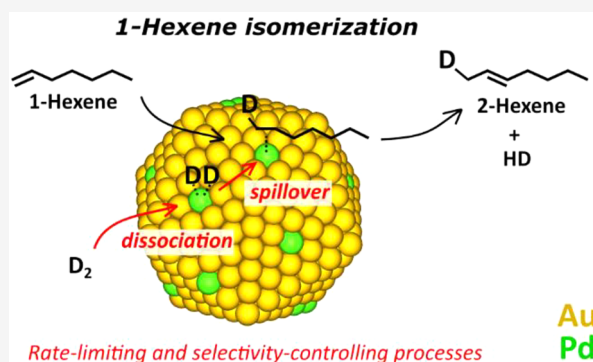
INTRODUCTION

Selective alkyne and alkene hydrogenation reactions are key processes in the chemical industry, for instance, in purifying alkene feedstocks for polymer production. Trace amounts of alkyne and diene impurities in the monoalkene feeds can substantially poison the polymerization catalysts further downstream. Selective hydrogenation of these impurities to monoalkenes is typically used to solve this problem. Pd-based materials are currently the state-of-the-art catalysts for this process due to their high catalytic activity at low temperatures.[1,2] However, the selectivity of these catalysts tends to deteriorate at low impurity levels, giving rise to the undesired conversion of valuable monoalkenes to fully hydrogenated alkanes.[3,4] Combining Pd with a less reactive but more selective second metal (Au, Ag, or Cu) can prevent such overhydrogenation.[4−12] A dilute alloy design in which Pd is doped into a coinage metal host is a particularly promising catalyst design for steering the selectivity in alkyne and diene hydrogenation to monoalkene isomers while maintaining high conversion. Successful examples include PdAu,[4,6−8,13] PdAg,[9,10] and PdCu[11,12] dilute alloy systems, yet our

mechanistic understanding as to why the alkene selectivity is improved on these dilute alloy surfaces is still incomplete.

An important step in the further improvement of the selectivity in alkyne and alkene hydrogenation lies in understanding how dilute alloys prevent the hydrogenation of the monoalkenes and why they favor alkene isomerization over alkene hydrogenation. On pure transition-metal surfaces, alkene isomerization and hydrogenation proceed via a Horiuti−Polanyi (HP) mechanism.[14−16] This mechanism consists of five key steps: (i) alkene adsorption, (ii) hydrogen adsorption and dissociation on the catalyst surface, and (iii) the addition of a dissociated hydrogen atom to the adsorbed alkene to form an alkyl intermediate, followed by either (iv) the addition of another dissociated hydrogen atom forming the alkane or (v) H-elimination from the alkyl intermediate to
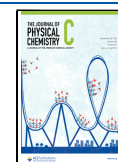
reform a double bond yielding an alkene isomer. The HP mechanism has been established for alkene hydrogenation on various monometallic surfaces using isotope-exchange reactions.[15,16] In this mechanism, the coverage of the reactants is considered to be particularly important to the selectivity: strong binding of the alkene and high hydrogen coverages lead to undesired alkane formation.[17,18] Diluting Pd in a coinage metal host was reported to prevent alkane formation due to weakening of the alkene adsorption energies on the Pd surface atoms[4,13,19] and/or by inhibiting Pd-hydride formation, where the hydrogen dissociation rate and binding strength can be modulated via the Pd ensemble size.[20−22] However, the adsorption of the reactants on the catalyst surface is only the first step in a more complex reaction mechanism consisting of numerous elementary steps that can all impact the catalyst selectivity and activity. How these elementary reaction steps occur on dilute alloy surfaces, which of the steps are rate-limiting, and whether the mechanism for alkene hydrogenation/isomerization is similar on dilute alloy- and monometallic surfaces are still unclear.

In this study, we combine experiment and theory to unravel the reaction mechanism and the rate-limiting and selectivity-controlling steps of 1-hexene hydrogenation/isomerization over a dilute Au-in-Pd alloy nanoparticle catalyst with the main objective being to understand the favorable selectivity of dilute alloys for hexene isomerization and their ability to prevent the hydrogenation to hexane. Isotopic labeling experiments in combination with density functional theory calculations and microkinetic modeling provided insight into the reaction mechanism, associated energy barriers, and rate-limiting and selectivity-controlling processes and established the key differences between the dilute Pd-in-Au alloy and monometallic Pd nanoparticle catalysts.

■ METHODS

Chemicals. All chemicals were used as received without further purification. Hydrogen tetrachloroaurate trihydrate ($HAuCl_4 \cdot 3H_2O$, ≥99.9%), sodium borohydride ($NaBH_4$, 99%), sodium tetrachloropalladate (Na_2PdCl_4, ≥99.99%), palladium nitrate hydrate ($Pd(NO_3)_2 \cdot xH_2O$), sodium citrate tribasic dihydrate (≥99.0%), potassium carbonate (K_2CO_3, ≥99.0%), tannic acid, L-ascorbic acid (≥99.0%), polyvinylpyrrolidone (PVP, $M_w \approx 55\,000$ g/mol), styrene (containing 4-*tert*-butylcatechol as a stabilizer, ≥99%), and tetraethyl orthosilicate (TEOS, 98%) were purchased from Sigma-Aldrich. Absolute ethanol (EtOH) was purchased from KOPTEC. Ultrapure water (Millipore Milli-Q grade, MQ) with a resistivity of 18.2 MΩ was used in all of the experiments. All glassware for the AuNP synthesis was cleaned with fresh aqua regia (HCl/HNO_3 in a 3:1 volume ratio), rinsed with large amounts of water, and dried at 403 K before use.

Catalyst Synthesis. The synthesis of the Pd_4Au_{96} and Pd RCT catalysts is described by van der Hoeven et al.[21] In short, the preparation is a multistep colloidal synthesis consisting of gold nanoparticle synthesis, the attachment of the gold nanoparticles to polystyrene colloids creating so-called raspberry colloids, Pd overgrowth on the gold nanoparticles, the assembly of the raspberry colloids into a colloidal crystal, infiltration of the interstitials with a silica sol gel, and finally a calcination step to remove the polystyrene colloids, rendering a solidified, microporous silica framework with the Pd_4Au_{96} and Pd NPs embedded in the pore walls.[24]

The gold nanoparticles for the Pd_4Au_{96} sample were synthesized using a procedure from Piella et al.[37] on a 450 mL scale at 343 K. The reaction mixture contained 0.30 mL of 2.5 mM tannic acid, 3.0 mL of 150 mM K_2CO_3, and 4.5 mL of 25 mM $HAuCl_4$ in H_2O. The Pd particles were synthesized on a 212 mL scale at 273 K under Ar.[4] The reaction mixture contained 200 mL of MQ H_2O, 10 mL of aqueous PVP solution (5.2 g PVP in 10 mL MQ H_2O), 1.0 mL of 0.14 mM $Pd(NO_3)_2$ in water, and 1.0 mL of 2.2 mM $NaBH_4$ in ice-cold MQ H_2O. After the reaction solution was stirred at 273 K for 30 min, it was aged for 48 h at room temperature.

The raspberry colloids were prepared by attaching the gold and palladium nanoparticles to the sacrificial polystyrene (PS) colloids (d_{PS} = 393 nm). To 150 mL of AuNPs, 1.5 mL of an aqueous PVP solution (0.1 g PVP per mL H_2O) and 12 mL of thiol-functionalized PS colloids (5.0 wt % in water) were added. After washing three times with MQ H_2O, the colloids were redispersed in 12 mL of MQ H_2O.

The Pd growth on the AuNPs attached to polystyrene colloids occurred at low pH to ensure sufficiently slow reaction rates and selective growth on the AuNPs.[38] To 12 mL of a raspberry colloid dispersion (5.0 wt % PS in water), 150 mL of MQ H_2O, 1.5 mL of 0.1 M HCl, 120 μL of 10 mM Na_2PdCl_4, and 120 μL of 40 mM ascorbic acid were added to obtain the Pd_4Au_{96} NPs. The raspberry colloids were washed twice, redispersed in 12 mL of MQ H_2O, and dried at 338 K in air.

The dried colloidal crystal was infiltrated three times with 600 μL of a prehydrolyzed TEOS solution (33 vol % of a 0.10 M HCl in H_2O solution, 33 vol % ethanol, and 33 vol % TEOS).[23] Finally, the samples were calcined to remove PS colloids by heating them in static air from room temperature to 773 K at 1.9 K/min and held at 773 K for 2 h. Inductively coupled plasma mass spectrometry (ICP-MS, Agilent Technologies 7700x) was used for compositional analysis (metal composition and metal weight loading). The composition, weight loading, and nanoparticle size of the Pd_4Au_{96} sample were 3.6 atom % Pd, 4.2 wt %, and 4.9 ± 0.9 nm, respectively. The weight loading and nanoparticle size of the Pd sample were 0.6 wt % and 6.9 ± 2.1 nm, respectively.

Catalysis Experiments. Prior to catalysis, the RCT catalysts were sieved (100−300 μm). The Pd and Pd_4Au_{96} RCT catalysts, 10 and 20 mg, respectively, were loaded into a cylindrical quartz reactor tube with an inner diameter of 1 cm. The catalysts were diluted in quartz sand to obtain a 1 cm bed height. Pretreatment in 20% O_2 in Ar at a flow rate of 50 mL/min was carried out to segregate Pd to the NP surface of the Pd_4Au_{96} nanoparticles. In short, the catalysts were heated to 773 K at 10 K/min and kept at 773 K for 30 min, followed by cooling in 40 mL/min Ar to 373 K. From 373 K to RT, the catalysts were cooled in 20% H_2 in Ar to ensure the reduction of the Pd atoms. The reaction mixture was premixed on bypass for at least 2 h prior to the start of the experiment. In the steady-state 1-hexene hydrogenation experiments, the reaction mixture was composed of 1% 1-hexene, 20% H_2, or 20% D_2 in Ar with a total flow rate of 50 mL/min. The 1-hexene flow was achieved by evaporating 1-hexene using 2.1 mL/min Ar flow at room temperature (yielding a 1-hexene flow of 0.5 mL/min).

The reaction products were analyzed using both an online mass spectrometer (Hiden HAL 301/3F series) and an online gas chromatograph−mass spectrometer (Agilent 7890A series GC, Agilent 5975C series MS). The separate mass spectrometer was used to monitor m/z = 2, 3, 4, 40, 69, and 70 corresponding to H_2, HD, D_2, Ar, 1-hexene (-d_0) and 1-

hexene (d_1), respectively. The inlet pressure for the MS was set at 9×10^{-7} Torr, and the scan rate was typically 0.1−1 channel/s. The sensitivity of the MS for each m/z value was set between −7 and −10 depending on the concentration of each component in the reaction mixture.

Quantitative Gas Chromatography Mass Spectrometry Analysis. The mass spectrometer data were used to quantify the HD ($m/z = 3$) to D_2 ($m/z = 4$) ratio according to the procedure reported in ref 21. The GC−MS data were used to quantify the amount of 1-hexene, cis-2-hexene, trans-2-hexene, 3-hexene, and n-hexane and the number of deuterium atoms incorporated in each of these products. cis- and trans-3-hexene are grouped together as 3-hexene because these isomers could not be analyzed separately. The 1-hexene conversion levels were calculated based on the GC−MS data using the following formulas:

$$\text{conversion}(\%) = \frac{\text{products}}{\text{reactant + products}} \times 100\%$$

$$\text{products} = \frac{A_{cis\text{-}2\text{-hexene}}\, x_{cis\text{-}2\text{-hexene}}}{\sigma_{\text{hexene}}}$$
$$+ \frac{A_{trans\text{-}2\text{-hexene}}\, x_{trans\text{-}2\text{-hexene}}}{\sigma_{\text{hexene}}}$$
$$+ \frac{A_{3\text{-hexene}}\, x_{trans\text{-}2\text{-hexene}}}{\sigma_{\text{hexene}}} + \frac{A_{n\text{-hexene}}\, x_{n\text{-hexane}}}{\sigma_{\text{hexane}}}$$

$$\text{reactant} = \frac{A_{1\text{-hexene}}\, x_{1\text{-hexene}}}{\sigma_{1\text{-hexene}}}$$

In H_2, A is the area under the peak in the GC spectrum for $m/z = 84$ for 1-hexene, cis-2-hexene, trans-2-hexene, and 3-hexene and in the GC spectrum for $m/z = 86$ for n-hexane peaks. In D_2, A is the area under the peak in the GC spectra for $m/z = 84$ (d_0), 85 (d_1), 86 (d_2), 87 (d_3), and 88 (d_4) for the 1-hexene, cis-2-hexene, trans-2-hexene, and 3-hexene isotopologues and for $m/z = 86$ (d_0), 87 (d_1), 88 (d_2), 89 (d_3), and 90 (d_4) for the n-hexane isotopologues. σ is the ionization cross section which is 16.3 for 1,2,3-hexene and 19.4 for n-hexane.[39] x is a correction factor to calculate the area under the peak of the total GC spectrum (with all m/z values included) from the areas in the GC spectra at $m/z = 84$ and 86 for 1,2,3-hexene and n-hexane, respectively. These correction factors were determined by injecting 1-hexene, cis-2-hexene, trans-2-hexene, 3-hexene, and n-hexane separately in the GC−MS and measuring the total and separate m/z GC spectra (example shown in Figure S10). Table 1 lists the correction factors used. Figure S11 shows an example set of GC−MS spectra used for

Table 1. Correction Factors (x) Used to Compute the Areas under the Peak for the Hexenes and n-Hexane in the Total GC Spectra (Including All m/z Values) From Their Areas in the GC−MS Spectra with $m/z = 84$ and 86, Respectively[a]

compound	correction factor (x)
1-hexene	17.66
cis-2-hexene	8.26
trans-2-hexene	7.95
3-hexene	8.14
n-hexane	24.30

[a]The correction factors were determined experimentally for the GC−MS used in this work.

the quantitative analysis of the number of deuterium atoms incorporated in the hexene isomers and in hexane.

DFT Calculations. All density function theory (DFT) calculations were performed using the Vienna ab initio simulation package (VASP).[40,41] The $Pd_1/Au(111)$ surface was constructed using a six-layer slab and a (4×4) unit cell. For this unit cell size, a Monkhorst−Pack-generated $7 \times 7 \times 1$ K-points grid was used.[42] A cutoff energy of 400 eV for the plane wave basis set and the optPBE-vdW functional were employed for all calculations.[43−45] During structural optimizations, the bottom four layers of the slab model were fixed in the Au bulk position, and the upper two layers and the adsorbates were allowed to relax until the force on each relaxed atom was smaller than 0.03 eV/Å. Transition states were located using both the dimer method and the quasi-Newton method.[46] For simplicity, free-energy calculations neglect the zero-point energy (ZPE) and the vibrational contribution for both the gaseous and surface species. The impact of the ZPE on the most important barriers (H_2 dissociation and H-migration from PdH_2) is small: the ZPEs on $H_2(g)$, TS-Dis, and H-migration from PdH_2 are 0.27, 0.27, and 0.26 eV, respectively.[28] Hence, the differences in the ZPE are small. All atomic configurations reported in this work were visualized using VESTA.[47]

Microkinetic Simulations. Microkinetic simulations were performed to compare the theoretically proposed reaction pathway to the experimentally observed catalyst reactivity, product selectivity, and degree of H/D exchange in 1-hexene, 2-hexene, and n-hexane. The kinetic rate parameters were computed from DFT energetics. The forward and reverse rate constants of surface reactions were computed using transition-state theory:[48]

$$k_i = \frac{k_B T}{h} \exp\left(\frac{-\Delta G^\circ_{\text{act}}}{RT}\right)$$

The rate constants for the adsorption of gas molecules were computed with the kinetic theory of gases[48]

$$k_{\text{ads},i} = \frac{\sigma A_{\text{site}} P^\circ}{\sqrt{2\pi m_i k_B T}}$$

where σ is the sticking coefficient, A_{site} is the area of the active site, P° is the standard state pressure (1 bar), m_i is the mass of the adsorbate i, and k_B is Boltzmann's constant.

For the simulations in this work, the sticking coefficient was assumed to be 1. The surface area of an active site was calculated using the experimental bulk lattice constants of Pd and Au (3.88 and 4.06 Å, respectively).[49] The atomic fraction of Pd in the alloy is set to 5%. Following Vegard's law, the area occupied by one atom on the (111) facet is 7.10×10^{-20} m^2. The corresponding rate constants of desorption were computed using the equilibrium constants of adsorption:

$$k_{\text{des},i} = \frac{k_{\text{ads},i}}{K_{\text{ads},i}}$$

$$K_{\text{ads},i} = \exp\left(-\frac{\Delta G^\circ_{\text{ads},i}}{k_B T}\right)$$

The rate of elementary step j was computed using the following equation
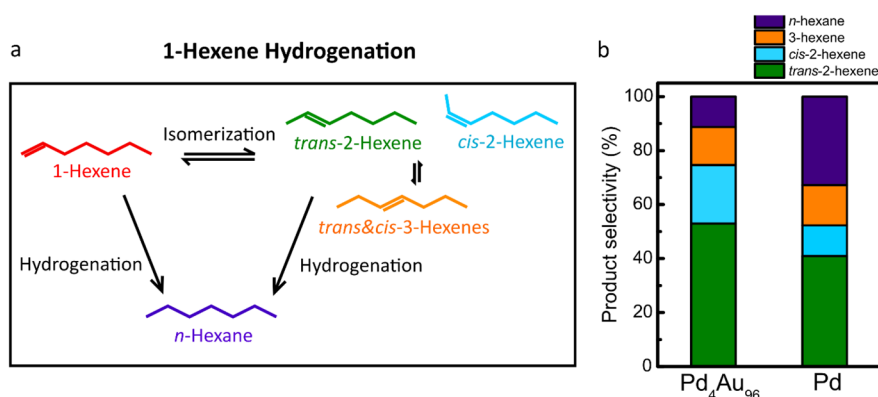
Figure 1. 1-Hexene hydrogenation over Pd_4Au_{96} and Pd catalysts renders different product distributions. (a) Reaction scheme for 1-hexene isomerization to (*trans-*, *cis-*) 2- or (*trans-*, *cis-*) 3-hexene and hydrogenation to *n*-hexane. (b) Product selectivity at 92% 1-hexene conversion for Pd_4Au_{96} and the Pd catalyst. The catalytic data were measured under steady-state conditions at 373 K (Pd_4Au_{96}) and 320 K (Pd) in 1 vol % 1-hexene and 20 vol % H_2 in Ar, with a total flow of 50 mL/min using a catalyst bed of 20 mg of 4.2 wt % Pd_4Au_{96} and 2 mg of 0.6 wt % Pd, corresponding to 16 and 12 μg Pd, respectively. *cis-* and *trans-*3-hexene are grouped together as 3-hexene because these isomers could not be analyzed separately.

$$r_j = k_j^{\text{fwd}} \prod_i \alpha_{i,\text{IS}}^{\nu_{ij}^{\text{fwd}}} \prod_i \alpha_{i,\text{gas}}^{\nu_{ij}^{\text{fwd}}} - k_j^{\text{rev}} \prod_i \alpha_{i,\text{IS}}^{\nu_{ij}^{\text{rev}}} \prod_i \alpha_{i,\text{gas}}^{\nu_{ij}^{\text{rev}}}$$

where k_j^{fwd} and k_j^{rev} are the forward and reverse rate constants and k_{ij}^{fwd} and k_{ij}^{rev} are the stoichiometric coefficients of reactant i in the forward and reverse directions. The activity α_i was assumed to be the surface coverage fraction θ_i for surface intermediates (including bare sites, normalized by the total number of sites) and as the ratio of the partial pressure to the standard pressure, $P_i/P°$, for gaseous species.[50]

The time-dependent coverages of surface intermediates are obtained as the steady-state solution of the following system of ordinary differential equations:

$$\frac{d\theta_i}{dt} = -\sum_j \nu_{ij}^{\text{fwd}} r_j + \sum_j \nu_{ij}^{\text{rev}} r_j$$

Following Wang et al., the steady-state solution is achieved in two steps.[28,51] Starting from a bare surface, the equations are first integrated over 500 s until they have approximately reached a steady state. The resulting coverages are then used as an initial guess of the numerical solution to the following equations:

$$0 = -\sum_j \nu_{ij}^{\text{fwd}} r_j + \sum_j \nu_{ij}^{\text{rev}} r_j,$$

$$\theta_{\text{Pd}}(t=0) = \sum_i \theta_{\text{Pd},i},$$

$$1 = \sum_i \theta_{\text{Pd},i} + \sum_i \theta_{\text{Au},i}$$

Here, $\theta_{\text{Pd},i}$ and $\theta_{\text{Au},i}$ are the surface coverages of species i on Pd and Au sites, respectively.

To evaluate the degree of H/D exchange in 1-hexene, 2-hexene, and *n*-hexane as a function of 1-hexene conversion, the above microkinetic model was embedded in an isothermal and isobaric plug-flow reactor (PFR). The metal content of the catalyst was assumed to be 4.2 wt %. Each Pd-in-Au nanoparticle in the catalyst was assumed to be a sphere 4.9 nm in diameter, with 5% of all atoms in each particle being Pd.

■ RESULTS

Selectivity Differences between the Pd-in-Au and Pd Nanoparticle Catalysts. The dilute Pd-in-Au and monometallic Pd nanoparticle catalysts were prepared using a raspberry colloid templated (RCT) approach.[23] This multistep colloidal synthesis route yields a well-defined, macroporous metal oxide support with partially embedded metal nanoparticles in the pore walls.[24] The partial embedding gives rise to a unique sinter-resistance of the nanoparticles at elevated temperatures (800 °C)[24] and under catalytic conditions,[25] ensuring stable conversions and minimal catalyst deactivation.[4,25] The robustness of the RCT catalysts makes them suitable systems for detailed catalytic model studies. Here, a monometallic RCT catalyst (Pd) and a dilute alloy catalyst were prepared with a nanoparticle composition of 4 atom % Pd and 96 atom % Au (Pd_4Au_{96}) embedded in a silica matrix.[21] The Pd and Pd_4Au_{96} catalyst had metal loadings of 0.6 and 4.2 wt %, respectively, and particle sizes of 6.9 ± 2.1 and 4.9 ± 0.9 nm, respectively.[21] The amount of catalyst loaded was adjusted to ensure a similar amount of Pd in each experiment: 12 and 16 μg of Pd for pure Pd and Pd_4Au_{96}, respectively. Prior to the catalytic testing for 1-hexene hydrogenation, the catalysts were activated via pretreatment in oxygen to segregate Pd to the surface of the dilute alloy catalyst (Methods).[26]

Testing of the monometallic Pd and bimetallic Pd_4Au_{96} catalyst in the selective hydrogenation of 1-hexene under steady-state conditions showed that the Pd_4Au_{96} nanoparticles preferentially converted 1-hexene to its isomers, (*trans-* and *cis-*) 2- and 3-hexene, whereas monometallic Pd exhibits a higher selectivity toward the fully hydrogenated *n*-hexane product. The reaction scheme in Figure 1a depicts the isomerization of 1-hexene to (*trans-* and *cis-*) 2- and 3-hexene and the hydrogenation of various isomers into *n*-hexane. The product distributions in Figure 1b show that the predominant product for both catalysts is *trans-*2-hexene and both catalysts produce a similar amount of 3-hexene. However, there is a clear difference in *n*-hexane selectivity: the Pd catalysts produced 33% *n*-hexane, which is 3 times more than the Pd_4Au_{96} catalyst (11% *n*-hexane). The product selectivity was deliberately compared at relatively high and equal 1-hexene conversion (92% in both cases), as maintaining high selectivity toward the hexene isomers is most difficult under these conditions and
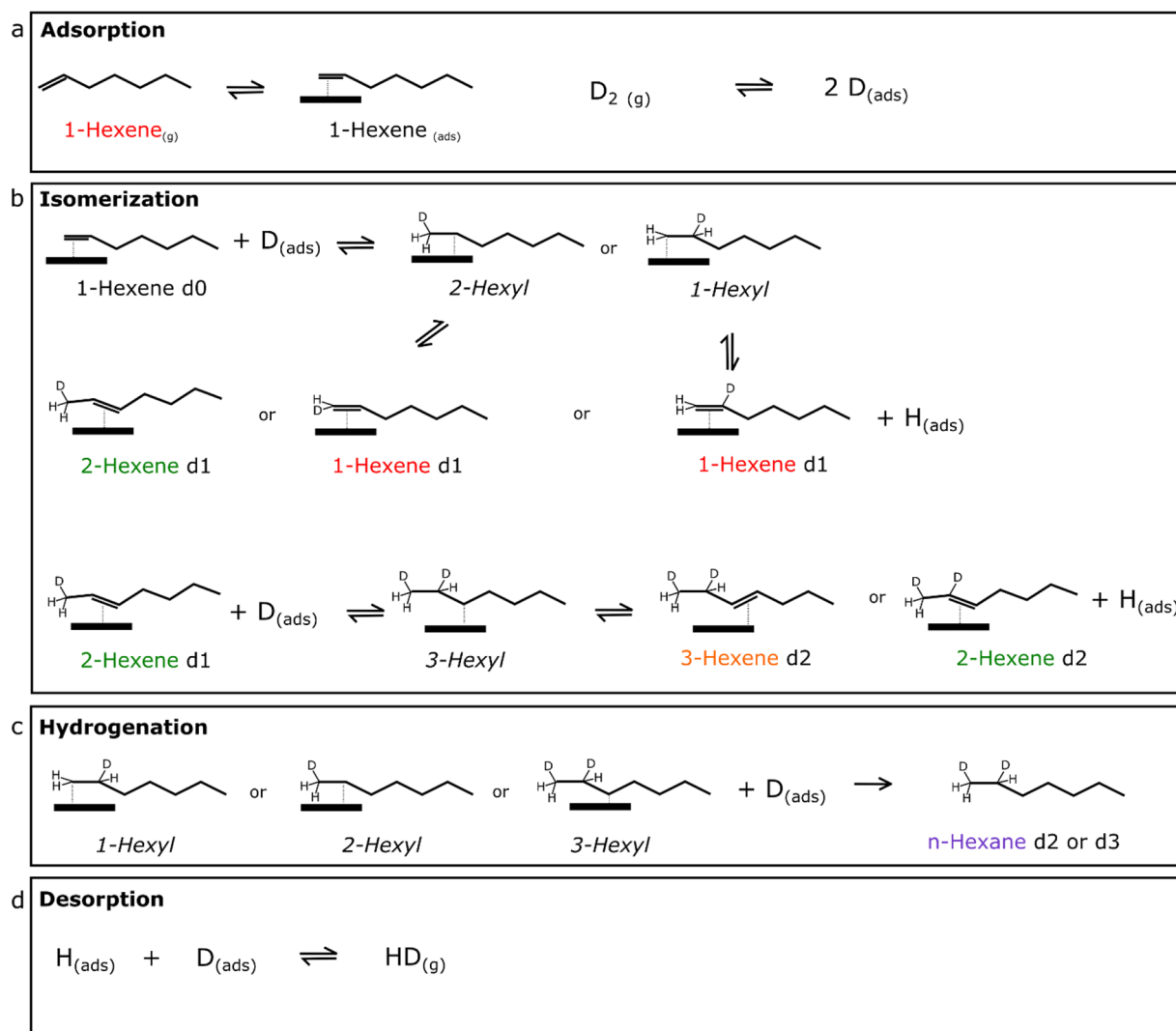
Figure 2. Isotopic labeling with deuterium provides mechanistic insight into 1-hexene hydrogenation. (a) Reaction diagram showing the adsorption of 1-hexene and the dissociative adsorption of D_2 on the catalysts surface. (b) Isomerization of 1-hexene to deuterium containing 1-, 2-, and 3-hexene. The 1-hexyl and 2-hexyl intermediates are formed upon D addition to the second and first carbon atoms, respectively, and lead to the formation of 1-, and 1- and 2-hexene, respectively. The formation of 3-hexene proceeds through the 3-hexyl intermediate which can form upon (re)adsorption of 2-hexene. (c) Hydrogenation of the hexyl intermediates (1-, 2-, or 3-hexyl) leads to the formation of the fully hydrogenated *n*-hexane product. (d) HD is formed when an adsorbed hydrogen atom originating from reversible hexene isomerization recombines with an adsorbed deuterium atom.

large differences in selectivity between palladium and bimetallic palladium−gold catalysts are typically observed at high conversion (i.e., low 1-hexene levels).[4] Note that the Pd catalyst exhibits a higher catalytic activity: 92% conversion was reached at 320 and 373 K for the Pd and Pd_4Au_{96} catalysts, respectively.

Mechanistic Insight via Isotopically Labeled 1-Hexene Hydrogenation. Isotopic labeling experiments using deuterium (D_2) instead of hydrogen (H_2) gas to hydrogenate 1-hexene were used to further investigate the observed differences in selectivity between the dilute alloy and monometallic Pd catalyst, and to establish whether both catalysts follow an HP mechanism. Specifically, the isotopic labeling experiments provide insight into (i) the reversibility of hexene isomerization (C=C bond position change) and (ii) the relative rate of isomerization versus hydrogenation over the mono- and bimetallic catalyst. Figure 2 shows the different reaction pathways and intermediates that can form in the

presence of D_2. The reaction starts with the adsorption of 1-hexene on the catalyst surface[4,6] and the dissociative adsorption of deuterium.[21] These two processes must occur on two separate Pd surface sites.[21] Next, one adsorbed deuterium atom migrates via the Au surface to the Pd site where 1-hexene is adsorbed. A 2- or 1-hexyl intermediate is formed via the addition of the migrated deuterium atom to the first or second carbon atom, respectively. These hexyl intermediates can either be further hydrogenated to *n*-hexane by the addition of a second deuterium atom (Figure 2c) or can lose a hydrogen atom to form 1- or 2-hexene (Figure 2b). 1-Hexene (d_1) can form from the 1- or 2-hexyl intermediate, whereas 2-hexene (d_1) needs to go via the 2-hexyl intermediate. The readsorption of 2-hexene and the formation of the 3-hexyl intermediate via the addition of a deuterium atom to the second carbon atom can lead to the formation of 3-hexene (d_2). Because the formation of 3-hexene proceeds via 2-hexene, a larger number of incorporated deuterium atoms
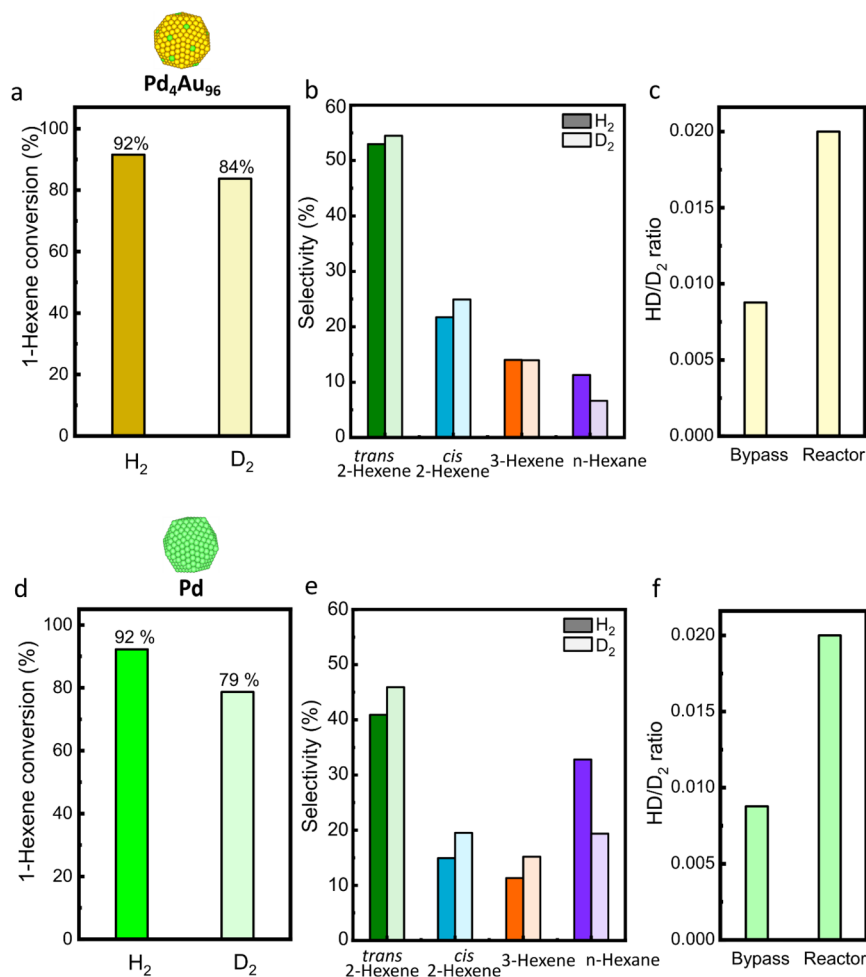
Figure 3. H/D addition to the hexene double bond is reversible on the Pd_4Au_{96} (a−c) and Pd (d−f) catalysts. (a, d) Steady-state 1-hexene conversion in H_2 and D_2 at 373 K (Pd_4Au_{96}) and 320 K (Pd) in 1 vol % 1-hexene, 20 vol % H_2, or 20 vol % D_2 in Ar, with a total flow of 50 mL/min using a catalyst bed of 20 mg of 4.2 wt % Pd_4Au_{96} and 2 mg of 0.6 wt % Pd. (b, e) Selectivity for *trans*-2-hexene, *cis*-2-hexene, 3-hexene, and *n*-hexane in H_2 (dark) and D_2 (light). (c, f) HD/D_2 ratio over the bypass and over the reactor during 1-hexene hydrogenation in D_2. The corresponding mass spectrometry data can be found in Figure S1.

are expected. Clear indications for reversible isomerization and an HP mechanism are (i) the formation of hexene isomers with one or more deuterium atoms incorporated, (ii) the formation of hexane with three or more deuterium atoms, and (iii) the formation of HD. Furthermore, the number of deuterium atoms incorporated in the hexene isomers is a qualitative measure of the number of double-bond formations from a hexyl isomer prior to the irreversible hydrogenation to *n*-hexane.

Quantitative Analysis of Deuterium-Labeled Hydrogenation Products. The isotopically labeled 1-hexene hydrogenation experiments were conducted under steady-state conditions and at high 1-hexene conversion (92%) to gain insight into the reaction mechanism over the Pd_4Au_{96} and Pd catalysts. Quantitative analysis of all products and the number of deuterium atoms incorporated was achieved by simultaneously using an online mass spectrometer to monitor the HD formation and a gas chromatography mass spectrometer (GC−MS) to quantify the hexene and hexane products (Methods). First, steady-state conditions in H_2 were ensured prior to exchanging the H_2 flow for D_2 flow (Figure S1). Upon switching to D_2, a slight drop in 1-hexene conversion was observed, from 92 to 84 and 79% for

Pd_4Au_{96} and Pd, respectively (Figure 3a,d). Additionally, a change in product selectivity occurred: the hexane fraction decreased whereas the hexene isomer fraction increased for both catalysts (Figure 3b,e). This change in product selectivity is mostly a conversion effect because the conversion vs product selectivity curves are nearly identical in H_2 and D_2 (Figure S2). Hence, the same preferences for Pd in *n*-hexane formation and Pd_4Au_{96} in isomer formation were preserved in D_2. In both cases, HD is formed, following from the increased HD/D_2 ratio over the reactor with respect to the bypass (Figure 3c,f and Figure S3), which suggests reversible double-bond formation and an HP mechanism on both catalysts. Note that the 1-hexene hydrogenation activity of the Pd catalyst exceeds that of Pd_4Au_{96} catalysts: 25 vs 5 $mmol_{1-hexene}$ s^{-1} g_{Pd}^{-1} at 320 K (calculated from the data shown in Figures S4 and S5). Both catalysts are stable under steady-state conditions and during heating and cooling (Figures S4a and S5a).

The number of deuterium atoms incorporated in the hexene isomers and *n*-hexane at high steady-state conversion (Figure 4) and for the full range of conversion levels (Figures S4 and S5) can be summarized in five key findings. First, there is a clear isotope effect, where hydrogen incorporation is favored over deuterium incorporation. Only at very high conversions
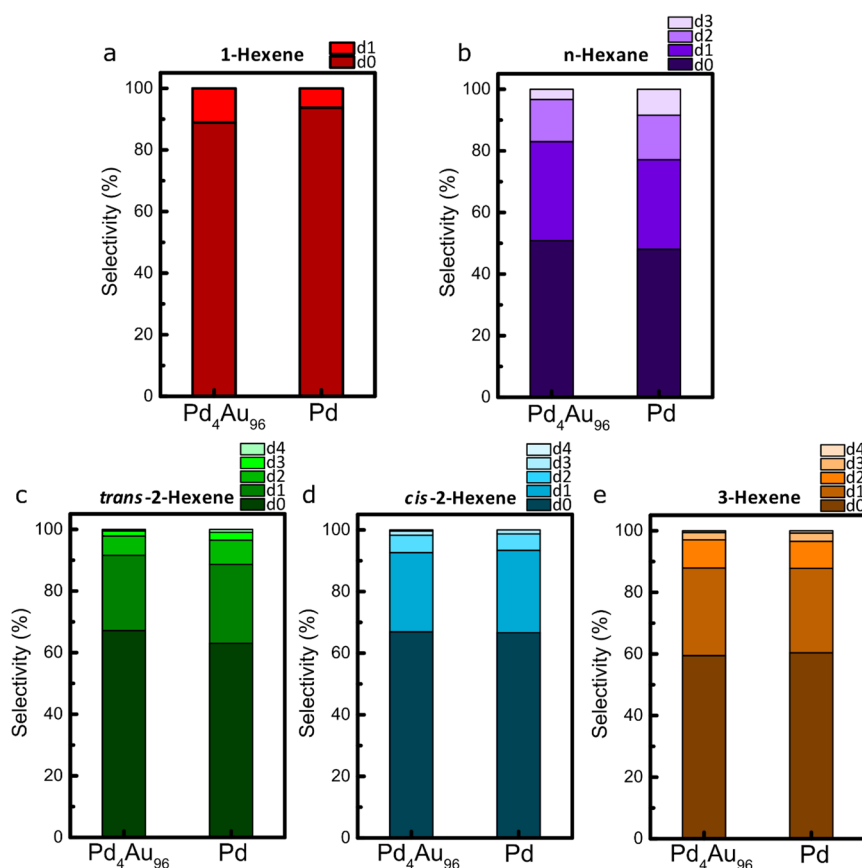
Figure 4. Deuterium incorporation in the hexene isomers and n-hexane for the Pd_4Au_{96} and Pd catalyst. Product selectivity to (a) 1-hexene d_0 and d_1, (b) n-hexane d_0-d_3, (c) $trans$-2-hexene d_0-d_4, (d) cis-2-hexene d_0-d_4, and (e) 3-hexene d_0-d_4. The catalytic data were measured under steady-state conditions at 373 K (Pd_4Au_{96}) and 320 K (Pd) in 1 vol % 1-hexene and 20 vol % D_2 in Ar, with a total flow of 50 mL/min using a catalyst bed of 20 mg of 4.2 wt % Pd_4Au_{96} and 2 mg of 0.6 wt % Pd.

do the number of deuterium atoms increase and does the fraction of deuterated products (d_1-d_4) exceeds that of d_0 products (Figures S4 and S5). Mass balance calculations confirmed that the H_{ads} needed to form the 2-,3-hexene and n-hexane d_0 products is supplied via the hydrogen atoms released upon hexene isomerization. Second, there is a clear difference in deuterium incorporation in 1-hexene between the Pd and Pd_4Au_{96} catalysts (Figure 4a). The fraction of 1-hexene d_1 was lower for the Pd catalyst (Figure S5c) and decreased with increasing conversion, whereas an increase was observed for the Pd_4Au_{96} catalyst (Figure S4c). This implies that the probability of forming 1-hexene from the 1-, or 2-hexyl intermediate is lower on a Pd than on a Pd_4Au_{96} surface. Third, the number of deuterium atoms incorporated in n-hexane is higher for the Pd compared to the Pd_4Au_{96} catalyst (Figure 4b), indicating a higher concentration of adsorbed deuterium atoms on the Pd surface and/or a higher probability for hydrogenation vs isomerization to occur. Fourth, a slightly higher deuterium incorporation in $trans$-2-hexene for the Pd versus the Pd_4Au_{96} catalyst was observed (Figure 4c), suggesting either that more isomerization cycles occur on the Pd surface due to the longer residence time of the intermediate and/or there is a higher supply of dissociated D vs dissociated H on the catalyst surface. Fifth, the number of deuterium atoms incorporated in 1-hexene (Figure 4a) is substantially lower than in 2- (Figure 4d) and 3-hexene (Figure 4e), indicating that reversible isomerization back to 1-hexene is less likely than isomerization to 2- and 3-hexene. For both catalysts,

more deuterium was incorporated in 3-hexene, which is due to the fact that 3-hexene formation proceeds in two steps via 2-hexene formation.

Adsorption, Isomerization, and Hydrogenation Energies from First-Principles Calculations. Both 1- and 2-hexene bind more strongly on pure Pd than on Pd-doped Au, based on density functional theory calculations (DFT) on Pd(111) and $Pd_1Au(111)$ models (Table 2; Figure 5). Hence,

Table 2. Adsorption Internal Energies of 1- and 2-Hexene on a Monometallic Pd(111) and Single Pd Atom on the Au(Pd_1Au, 111) Surface[a]

	1-hexene	2-hexene
Pd_1Au	−1.22 eV	−0.93 eV
Pd	−1.67 eV	−1.45 eV

[a]The values were computed using density functional theory (DFT) calculations.

desorption of the 1- and 2-hexene is more facile from $Pd_1Au(111)$. The adsorption internal energies of 1- and 2-hexene were calculated for a single Pd atom on a face-centered-cubic (FCC) Au(111) surface ($Pd_1Au(111)$) and on a monometallic Pd(111) surface. A (111) surface termination was assumed as the nanoparticles in the catalysts exhibit a penta-twinned crystal structure with predominantly (111) facets at the nanoparticle surface.[21,24] Previous CO-DRIFTS
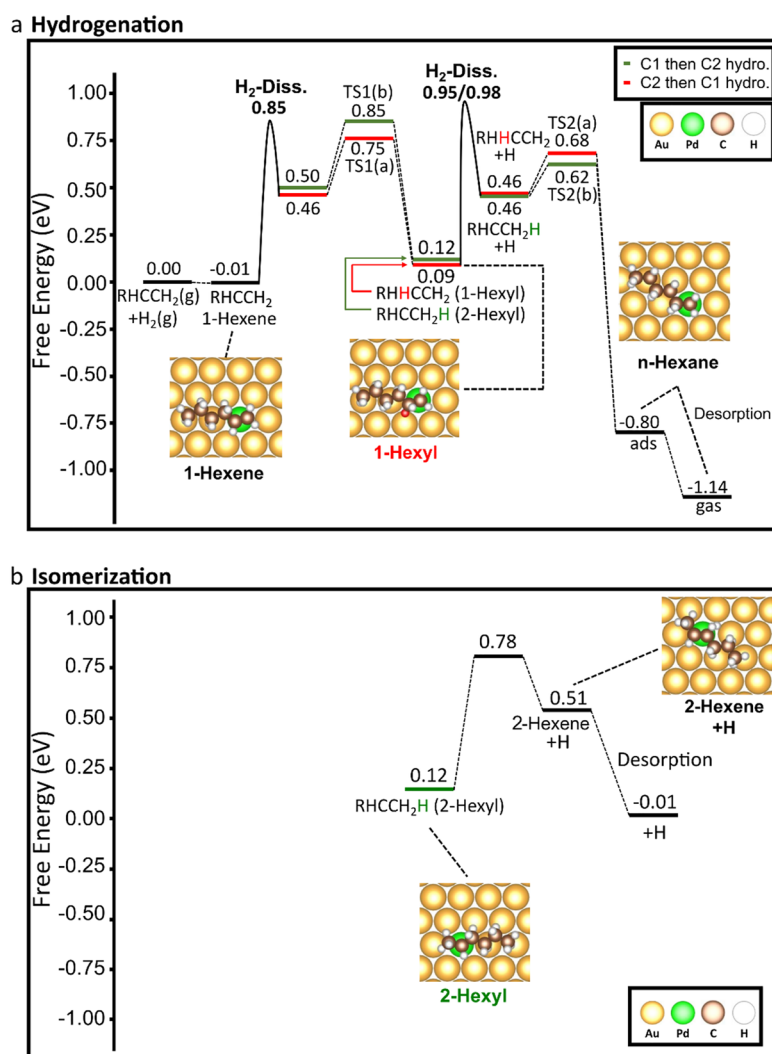
Figure 5. Free-energy profiles for (a) 1-hexene hydrogenation and (b) isomerization to 2-hexene calculated using DFT. The abbreviation R represents the butyl group attached to the C=C bond. Two different hydrogenation pathways are shown in (a): the green pathway first hydrogenates the terminal carbon atom of 1-hexene to form 2-hexyl while the red pathway first hydrogenates the carbon atom which is attached to the butyl group R to form 1-hexyl. Both pathways finish by hydrogenating the remaining unsaturated carbon atom in the hexyl intermediates. The H atoms newly added to the unsaturated hydrocarbons are denoted in red or green. (b) Isomerization pathway of the 2-hexyl intermediate to 2-hexene. Reaction conditions are $T = 363$ K, $P(H_2) = 0.2$ bar, $P(\text{1-hexene}) = 0.01$ bar, $P(\text{2-hexene}) = 0.001$ bar, and $P(n\text{-hexane}) = 0.001$ bar.

experiments showed that the surface composition of Pd_4Au_{96} in silica RCT catalysts mainly consist of Pd-monomers.[27]

The adsorption and dissociation of the hydrogen on Pd_1Au and Pd surfaces have previously been studied using experiment and theory.[21,28] Hydrogen dissociation is barrierless on Pd but rate-limiting on a Pd_1Au surface, leading to lower H/D coverages. Both the weaker hexene adsorption and the lower H/D coverages could explain the high hexene product selectivity and the reduced catalytic activity observed for the Pd_4Au_{96} catalyst in the experiment.

The free-energy profiles for 1-hexene hydrogenation to n-hexane (Figure 5a) and for isomerization to 2-hexene (Figure 5b) reveal that on the Pd_1Au surface the isomerization pathway is favored over hydrogenation to n-hexane. The full set of adsorption configurations of the reactants, intermediates, and products corresponding to the states in the energy profiles is provided in Figure S6. Both the hydrogenation and isomerization pathways start with the adsorption of 1-hexene on the Pd_1 site, which is thermoneutral under the considered

conditions. This is followed by hydrogen dissociation on a different Pd site and the migration of a H atom to the Pd site where the 1-hexene is bound, a process with an overall barrier of 0.86 eV.[29] Subsequent addition of the dissociated hydrogen atom on either the first or second carbon atom leads to the formation of the 2-hexyl (green) and 1-hexyl (red) intermediate, respectively. Next, the hexyl intermediates can be hydrogenated by the spillover of another H atom to the Pd site and adding a H atom to the remaining carbon radical/remaining unsaturated carbon of the hexyl intermediate to form n-hexane. The effective free-energy barrier for this process is 0.86 eV (H_2 dissociation). Alternatively, the reverse process from the hexyl intermediates to 1-hexene via reductive H-elimination can occur. The effective barrier for this reverse process is 0.67−0.73 eV (for 1-hexyl to TS1(a) and 2-hexyl to TS(b), respectively) and hence is lower than the effective barrier for hydrogenation to n-hexane. The barrier for isomerization to 2-hexene is even a bit lower, 0.66 eV, indicating that the formation of both 1- and 2-hexene is
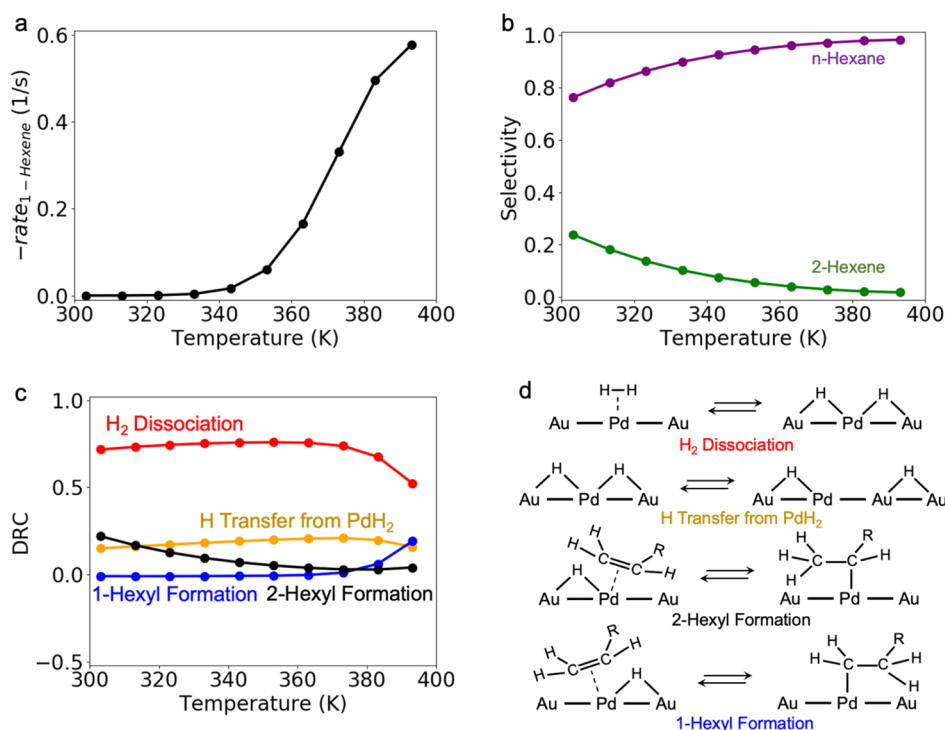
Figure 6. 1-Hexene consumption rate, product selectivity, and degrees of rate control (DRC) of transition states for 1-hexene consumption evaluated for the $Pd_1Au(111)$ model catalyst at fixed partial pressures. Microkinetic model of the 1-hexene reaction with H_2 evaluated at $p(H_2) =$ 0.2 bar, p(1-hexene) = 0.01 bar, and p(2-hexene) = p(n-hexane) = 0.001 bar. (a) Rate of 1-hexene consumption, (b) selectivity of 2-hexene and n-hexane formation, and (c) main rate-controlling transition states (TS) and their DRC for 1-hexene consumption as functions of temperature. (d) Schematic representations of the elementary steps corresponding to the transition states in panel (c). The reaction was found to start at ~350 K with 2-hexene as the minority product and H_2 dissociation as the main rate-controlling TS.

favored over the formation of n-hexane. Hence, the DFT calculations indicate that on the Pd_1Au surface backward dehydrogenation to form a hexene isomer is favored over hydrogenation to n-hexane and that isomerization to 2-hexene is favored over the reformation of 1-hexene. Both findings are in agreement with the experimental results for the Pd_4Au_{96} catalyst shown in Figures 1 and 4, respectively.

Microkinetic Simulations of 1-Hexene Hydrogenation. The reactivity and product selectivity of the calculated reaction mechanism for $Pd_1Au(111)$ were evaluated under the operating temperature and pressure using microkinetic models, which were parametrized using DFT-calculated reaction energies and barriers from Figure 5. In brief, the microkinetic model of 1-hexene hydrogenation/isomerization consists of four groups of reactions: (i) the dissociation of H_2 on a vacant Pd site and the exchange of atomic H between Pd sites, eventually also occupied by the hydrocarbon intermediate, via spillover on Au, (ii) the hydrogenation of 1-hexene to n-hexane through either the 1-hexyl or (iii) 2-hexyl intermediate, and (iv) the isomerization of 1- to 2-hexene through the 2-hexyl intermediate. The hydrogenation of hydrocarbon intermediates was assumed to take place only after hydrogen exchange. Table S1 summarizes all elementary steps, their kinetic rate constants, the Gibbs free energies of reaction, and the activation energies. At low 1-hexene conversion (fixed partial pressures of $p(H_2)$ = 0.2 bar, p(1-hexene) = 0.01 bar, and p(2-hexene) = p(n-hexane) = 0.001 bar), the conversion of 1-hexene started at 333 K, reaching a 1-hexene consumption rate of 0.331 s^{-1} at 373 K (Figure 6a), with 3% of the 1-hexene being isomerized to 2-hexene and the rest hydrogenated to n-

hexane (Figure 6b). Ninety-three percent of the produced n-hexane formed through the 1-hexyl intermediate, while the rest proceeded through the 2-hexyl intermediate. The discrepancy between the calculated product selectivity to preferential n-hexane formation and the experimental product selectivity to 2-hexene will be discussed later.

To identify the factors influencing the 1-hexene consumption rates and the 2-hexene selectivity, the degree of rate control (DRC) and degree of selectivity control (DSC) of transition states were computed. The DRC and DSC quantify the relative importance of surface intermediate and transition states to the overall reaction rate and product selectivity.[30] The calculated DRC of transition states (Figure 6c,d)[30] for 1-hexene consumption at 373 K and partial pressures corresponding to low 1-hexene conversion indicate that H_2 dissociation (DRC = 0.74) is the main rate-controlling TS, similar to that of 1-hexyne hydrogenation.[29] The TS of H transfer from the PdH_2 species onto the Au support is partially rate-controlling (DRC = 0.21), whereas the TS of C−H bond formation has only a very minor influence on the overall rate: DRC = 0.01 and 0.03 for the formation of 1-hexyl and 2-hexyl, respectively. The DSC showed that under the same conditions [T = 373 K, (H$_2$) = 0.2 bar, P(1-hexene) = 0.01 bar, and P(2-hexene) = P(n-hexane) = 0.001 bar] the TS of H_2 dissociation and that of H transfer to 2-hexyl to eventually form hexane (TS2(b)) and impact the selectivity of 2-hexene most negatively (Figure S7, DSC = −0.57 for both), meaning that if the energy of these TSs is lowered then the selectivity for 2-hexene decreases. On the other hand, the TS of 1-hexene hydrogenation to 2-hexyl (DSC = +0.93) and that of 2-hexyl
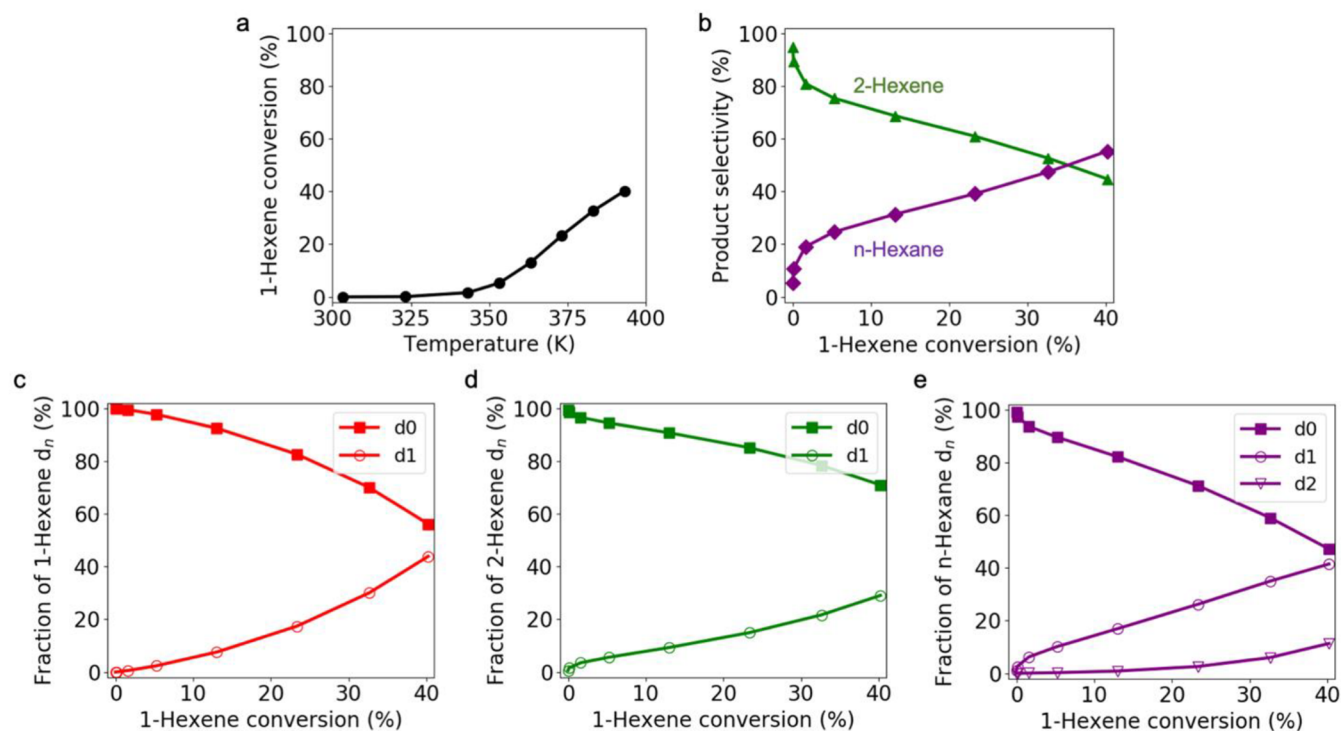
Figure 7. Product and isotope selectivity of 1-hexene deuteration and isomerization, with the barriers of H_2 dissociation and H-spillover increased by 0.1 eV. (a) 1-Hexene conversion and (b) selectivity of 2-hexene and *n*-hexane as functions of reactor temperature. (c) 1-Hexene isotope distribution, (d) 2-hexene isotope distribution, and (e) *n*-hexane isotope distribution as functions of 1-hexene conversion. The PFR, with 200 mg of catalyst loading, was assumed to operate at constant temperature and pressure (1 bar). The 1-hexene conversion and product/isotope selectivity were evaluated under an inlet flow of 50 standard mL/min (corresponding to the standard condition of $T = 273.15$ K and $P = 1$ atm), consisting of 1 vol % 1-hexene and 20 vol % D_2 with an inert balance.

dehydrogenation to 2-hexene (DSC = +0.69) positively influence the selectivity for 2-hexene (decreasing the energy favors the selectivity to 2-hexene).

The calculated DSCs and DRCs unambiguously show that the free-energy barriers of H_2 dissociation and H-spillover are critical in controlling the overall reactivity and selectivity of the catalyst. This is in line with the rate-controlling step in the partial hydrogenation of 1-hexyne over Pd_1/Au, where high H_2 dissociation and H-spillover free-energy barriers result in the reversible formation of hexyls on Pd_1 sites, boosting the catalyst's selectivity for 1-hexene by hindering the further hydrogenation of hexyls.[29] Here, the large H_2 dissociation and H-transfer barriers impact the selectivity in a similar way: 1-hexene isomerization becomes favored when further hydrogenation of hexyl intermediates is hindered by large H_2 dissociation barriers. To test the importance of the barriers beyond a local derivative in the DRCs and DSCs, the rates of 1-hexene conversion and product selectivity were recalculated after increasing the barrier of the H_2 dissociation and H-spillover steps by 0.1 eV (Figure S8). The recalculated 2-hexene selectivity is in much better agreement with experimental observations, where 2-hexene was found to be the majority product, and this will be further discussed below.

Theoretical Assessment of H/D Exchange in 1-Hexene Hydrogenation. To further strengthen the argument that large H_2 dissociation and H-spillover barriers are responsible for the high selectivity to 2-hexene, the microkinetic models were extended to include D_2/HD adsorption, D exchange between Pd/Au sites, and the deuteration of hydrocarbon intermediates (Table S1). For 1- and 2-hexene,

one H atom was allowed to be exchanged for D, while for *n*-hexane, up to two H atoms were allowed to be exchanged for D. To assess the degree of H/D exchange in the hexenes and *n*-hexane as a function of temperature and 1-hexene conversion, the microkinetic model was embedded in an isothermal and isobaric plug flow reactor (PFR) with 200 mg of catalyst loading. The inlet flow rate to the reactor was assumed to be 50 standard mL/min (corresponding to the standard condition of $T = 273.15$ K and $P = 1$ atm), consisting of 1 vol % 1-hexene and 20 vol % D_2 with an inert balance. The reactor simulations were first performed without any shift to the barriers of H_2 dissociation and H spillover (Figure S9). Following the 1-hexene consumption rates and 2-hexene selectivity evaluated at fixed partial pressures (Figure 6), *n*-hexane was found to be the major product. Marked H/D exchange was observed in the hydrocarbon species, with *n*-hexane d_1 as the most prevalent product at 10% 1-hexene conversion.

With the barriers of H_2/D_2/HD dissociation and H/D spillover increased by 0.1 eV, the simulated product selectivity qualitatively agrees with experimental observations (Figure 7). 1-Hexene conversion started at 343 K, with its overall conversion rising to 40.2% at 393 K (Figure 7a). In the temperature range of 303 to 383 K, 2-hexene was found to be the major product at most temperatures (Figure 7b), which is in agreement with experimental observation. At 373 K, the conversion of 1-hexene was 23.3%, with a 60.9% selectivity for 2-hexene. The calculated degree of H/D exchange (Figure 7c−e) also followed the trend observed in the experiment (Figure S4c). The amount of deuterated hexenes and *n*-hexane

increased from 303 to 393 K but never overtook the quantity of nondeuterated carbonaceous species. Similar to the experimental findings (Figure 4), the microkinetic modeling results at 373 K indicate that the majority of all carbonaceous species in the reactor outlet remained d_0: 82.6% 1-hexene d_0, 85.1% 2-hexene d_0, and 71.2% n-hexane d_0.

DISCUSSION

The isotope-exchange experiments indicate that 1-hexene hydrogenation on the dilute Pd_4Au_{96} alloy catalysts follows the same reaction mechanism as on the pure Pd nanoparticle catalyst. The formation of HD, incorporation of deuterium in hexene isomers, and formation of n-hexane with more than two deuterium atoms all support a Horiuti−Polanyi mechanism where alkene isomerization is reversible due to sequential hydrogen/deuterium addition and subtraction. So far, the HP mechanism had been established on pure metal systems[14−16] and was assumed to be extendable to bimetallic surfaces,[4] but to the best of our knowledge it has not been experimentally verified on bimetallic dilute alloy surfaces.

Our combined DFT and microkinetic modeling approach revealed that the preferential hexene isomerization of the Pd_4Au_{96} catalysts is likely caused by H_2 dissociation and H spillover being rate-limiting on the $Pd_1Au(111)$ alloy surface. The high selectivity toward the hexene isomers arising from a high H_2 dissociation barrier can be rationalized by the fact that hexane formation is hampered due to the limited availability of dissociated hydrogen on the alloy surface. The impact of the H spillover can be explained by the fact that H_2 dissociation must occur on an empty Pd site, and H spillover across the surface onto Au must occur to hydrogenate the C6 intermediates on another Pd site. A higher barrier for H spillover limits the amount of H transfer from one Pd site to an adsorbed 2-hexyl intermediate on a different Pd site. The latter process has a negative DSC. Hence, increasing the barrier H/D spillover improves the selectivity for 2-hexene.

The microkinetic modeling was essential in further establishing that the height of the H_2 dissociation and H-spillover barriers strongly impacts the product selectivity and that these energy barriers were likely underestimated in the DFT calculations because the product selectivity and deuterium incorporation did not match the experimental findings. Increasing the H_2 dissociation and H-spillover barriers by only 0.1 eV led to significantly better correspondence between the modeled and experimental hexene/hexane product selectivity as well as the deuterium distributions in these products, illustrating the added value of the isotopic labeling experiments in correctly correlating experiment and theory. One can note that 0.1 eV is within the error bar of DFT so that such a shift does not contradict our overall model. The preferential H incorporation in the hexene isomers and n-hexane also supports the argument that H_2/D_2 dissociation is rate-limiting on the Pd_4Au_{96} nanoparticle catalyst, and the larger number of deuterium atoms incorporated into n-hexane for pure Pd points toward a larger supply of dissociated D_2 on the Pd surface. Finally, the lower catalytic activity per Pd atom in the dilute alloy catalyst with respect to monometallic Pd also supports the fact that H_2 dissociation is rate-limiting on the dilute alloy catalysts, as the microkinetic modeling results in Figures 6 and 7 show that increasing the barrier for H_2 dissociation decreases the activity of the dilute alloy catalyst.

Lower alkene adsorption energies or the absence of a Pd-hydride phase is often invoked to explain the improved alkene selectivity of dilute alloy systems.[13,18] Indeed, our DFT calculations support a weakening of the alkene adsorption energies on dilute alloy surfaces (Table 2), which is in line with previous experimental findings where the ethylene adsorption energy decreased when diluting Pd in Au and when lower coverages of ethylene were measured with microcalorimetry.[13] However, the free-energy profiles and our microkinetic simulations show that this is not the main reason for the improved selectivity of dilute alloys. The preferential isomerization of the hexyl intermediates on dilute alloys is mainly due to the larger energy barrier for hydrogenation induced by the high energy barrier for H_2 dissociation and H spillover. The formation of the Pd-hydride is likely prevented in the dilute alloy design because three-dimensional Pd clusters are needed to accommodate such a phase,[31,32] which are unlikely to exist in a Pd_4Au_{96} system.[21] Interestingly, the isotope-exchange experiments do not show obvious indications that hydride formation plays an important role in the selectivity of the Pd catalyst either: no large increase in the deuterium incorporation is observed compared to Pd_4Au_{96} (Figures S4 and S5), which would be the case if a large excess of dissociated deuterium was stored in the Pd subsurface.

The findings of this study provide important guidelines for the design of dilute alloy catalysts with an optimized catalytic selectivity and activity for alkene hydrogenation/isomerization. Our work suggests that two key parameters need to be considered: (i) the energy barrier for hydrogen dissociation on the minority metal and (ii) the energy barrier for hydrogen spillover onto the metal host. Increasing the H_2 dissociation and H-spillover barrier induces a higher selectivity toward the isomerization products but lowers the overall catalytic activity. Hence, balancing these two parameters is key, which can be achieved via the Pd ensemble size and the choice of the metal host. Recent studies demonstrated that the hydrogen dissociation rate and binding strength can be tuned via the Pd ensemble size, where larger ensembles favor faster hydrogen dissociation and stronger hydrogen binding.[21,28] Subsequent hydrogen spillover can be optimized via the choice of the metal host, where H spillover is known to occur easily onto a Cu host,[12,33] and hydrogen spillover onto Ag^{31} and $Au^{6,20,34}$ surfaces occurs at sufficiently high pressures or in the presence of a more strongly binding reactant.

CONCLUSIONS

In this study, we presented new mechanistic insight to unravel the enhanced alkene selectivity of dilute alloy catalysts and their ability to prevent 1-hexene hydrogenation under hydrogen. By combining isotope-exchange experiments, DFT calculations, and microkinetic modeling, we show that hexene isomerization and hydrogenation on a dilute Pd-in-Au alloy catalyst occur via the same Horiuti−Polanyi mechanism as on a monometallic Pd surface and that the rate-limiting- and selectivity-controlling elementary steps are H_2 dissociation and H spillover onto the Au host. Importantly, hexene adsorption and H_2 dissociation cannot occur on the same Pd site, thus H migration is a key step in hexene conversion on the dilute alloys. Hydrogenation is prevented by the relatively high barrier for H_2 dissociation and H spillover, which is different from the common assumption that the enhanced alkene selectivity of Pd alloys originates from the weakening of the alkene adsorption energies. Our results have direct implications

for the future design of more efficient alloy catalysts for alkyne and alkene hydrogenation, where optimized selectivity and activity can be achieved via careful tuning of the Pd ensemble size and the choice of the host metal to control hydrogen dissociation and spillover.

ASSOCIATED CONTENT

Supporting Information

The Supporting Information is available free of charge at https://pubs.acs.org/doi/10.1021/acs.jpcc.2c04982.

> Extended data of the catalytic measurements, schematics of the adsorption geometries used for the DFT calculations, and additional microkinetic modeling details and results (PDF)

AUTHOR INFORMATION

Corresponding Authors

Jessi E. S. van der Hoeven − *Department of Chemistry and Chemical Biology and Harvard John A. Paulson School of Engineering and Applied Sciences, Harvard University, Cambridge, Massachusetts 02138, United States; Materials Chemistry and Catalysis, Debye Institute for Nanomaterials Science, Utrecht University, 3584 CG Utrecht, The Netherlands;* orcid.org/0000-0001-9832-289X; Email: j.e.s.vanderhoeven@uu.nl

Cynthia M. Friend − *Department of Chemistry and Chemical Biology and Harvard John A. Paulson School of Engineering and Applied Sciences, Harvard University, Cambridge, Massachusetts 02138, United States;* orcid.org/0000-0002-8673-9046; Email: friend@fas.harvard.edu

Authors

Hio Tong Ngan − *Department of Chemical and Biomolecular Engineering, University of California, Los Angeles, California 90095, United States*

George Yan − *Department of Chemical and Biomolecular Engineering, University of California, Los Angeles, California 90095, United States*

Joanna Aizenberg − *Department of Chemistry and Chemical Biology and Harvard John A. Paulson School of Engineering and Applied Sciences, Harvard University, Cambridge, Massachusetts 02138, United States;* orcid.org/0000-0002-2343-8705

Robert J. Madix − *Harvard John A. Paulson School of Engineering and Applied Sciences, Harvard University, Cambridge, Massachusetts 02138, United States;* orcid.org/0000-0002-3132-2382

Philippe Sautet − *Department of Chemical and Biomolecular Engineering and Department of Chemistry and Biochemistry, University of California, Los Angeles, California 90095, United States;* orcid.org/0000-0002-8444-3348

Complete contact information is available at:
https://pubs.acs.org/10.1021/acs.jpcc.2c04982

Author Contributions

C.M.F., P.S., and R.J.M. guided the research. J.E.S.v.d.H. prepared and characterized the catalysts, as advised by J.A., conducted the catalysis experiments, and developed the quantitative data analysis. H.T.N. performed the DFT calculations. G.Y. performed the microkinetic modeling. All authors participated in discussions and the interpretation of the data. J.E.S.v.d.H wrote the manuscript, with contributions from all authors.

Notes

The authors declare no competing financial interest.

REFERENCES

(1) Molnár, Á.; Sárkány, A.; Varga, M. Hydrogenation of Carbon-Carbon Multiple Bonds: Chemo-, Regio- and Stereo-Selectivity. *J. Mol. Catal. A Chem.* **2001**, *173* (1−2), 185−221.

(2) Lindlar, H. Ein Neuer Katalysator Für Selektive Hydrierungen. *Helv. Chim. Acta* **1952**, *35* (2), 446−450.

(3) Silvestre-Albero, J.; Rupprechter, G.; Freund, H. J. Atmospheric Pressure Studies of Selective 1,3-Butadiene Hydrogenation on Well-Defined Pd/Al2O3/NiAl(110) Model Catalysts: Effect of Pd Particle Size. *J. Catal.* **2006**, *240* (1), 58−65.

(4) Luneau, M.; Shirman, T.; Foucher, A. C.; Duanmu, K.; Verbart, D. M. A.; Sautet, P.; Stach, E. A.; Aizenberg, J.; Madix, R. J.; Friend, C. M. Achieving High Selectivity for Alkyne Hydrogenation at High Conversions with Compositionally Optimized PdAu Nanoparticle Catalysts in Raspberry Colloid-Templated SiO2. *ACS Catal.* **2020**, *10* (1), 441−450.

(5) Zhang, L.; Zhou, M.; Wang, A.; Zhang, T. Selective Hydrogenation over Supported Metal Catalysts: From Nanoparticles to Single Atoms. *Chem. Rev.* **2020**, *120* (2), 683−733.

(6) Liu, J.; Uhlman, M. B.; Montemore, M. M.; Trimpalis, A.; Giannakakis, G.; Shan, J.; Cao, S.; Hannagan, R. T.; Sykes, E. C. H.; Flytzani-Stephanopoulos, M. Integrated Catalysis-Surface Science-Theory Approach to Understand Selectivity in the Hydrogenation of 1-Hexyne to 1-Hexene on PdAu Single-Atom Alloy Catalysts. *ACS Catal.* **2019**, *9* (9), 8757−8765.

(7) van der Hoeven, J. E. S.; Jelic, J.; Olthof, L. A.; Totarella, G.; van Dijk-Moes, R. J. A.; Krafft, J. M.; Louis, C.; Studt, F.; van Blaaderen, A.; de Jongh, P. E. Unlocking Synergy in Bimetallic Catalysts by Core-Shell Design. *Nat. Mater.* **2021**, *20* (9), 1216−1220.

(8) Kolli, N. El; Delannoy, L.; Louis, C. Bimetallic Au-Pd Catalysts for Selective Hydrogenation of Butadiene: Influence of the Preparation Method on Catalytic Properties. *J. Catal.* **2013**, *297*, 79−92.

(9) Rassolov, A. V.; Bragina, G. O.; Baeva, G. N.; Mashkovsky, I. S.; Stakheev, A. Y. Alumina-Supported Palladium-Silver Bimetallic Catalysts with Single-Atom Pd1 Sites in the Liquid-Phase Hydrogenation of Substituted Alkynes. *Kinet. Catal.* **2020**, *61* (6), 869−878.

(10) Pei, G. X.; Liu, X. Y.; Wang, A.; Lee, A. F.; Isaacs, M. A.; Li, L.; Pan, X.; Yang, X.; Wang, X.; Tai, Z.; Wilson, K.; Zhang, T. Ag Alloyed Pd Single-Atom Catalysts for Efficient Selective Hydrogenation of

Acetylene to Ethylene in Excess Ethylene. *ACS Catal.* **2015**, *5* (6), 3717−3725.

(11) Boucher, M. B.; Zugic, B.; Cladaras, G.; Kammert, J.; Marcinkowski, M. D.; Lawton, T. J.; Sykes, E. C. H.; Flytzani-Stephanopoulos, M. Single Atom Alloy Surface Analogs in Pd0.18Cu15 Nanoparticles for Selective Hydrogenation Reactions. *Phys. Chem. Chem. Phys.* **2013**, *15* (29), 12187−12196.

(12) Kyriakou, G.; Boucher, M. B.; Jewell, A. D.; Lewis, E. A.; Lawton, T. J.; Baber, A. E.; Tierney, H. L.; Flytzani-Stephanopoulos, M.; Sykes, E. C. H. Isolated Metal Atom Geometries as a Strategy for Selective Heterogeneous Hydrogenations. *Science (80-.).* **2012**, *335* (6073), 1209−1212.

(13) Pei, G. X.; Liu, X. Y.; Wang, A.; Li, L.; Huang, Y.; Zhang, T.; Lee, J. W.; Jang, B. W. L.; Mou, C. Y. Promotional Effect of Pd Single Atoms on Au Nanoparticles Supported on Silica for the Selective Hydrogenation of Acetylene in Excess Ethylene. *New J. Chem.* **2014**, *38* (5), 2043−2051.

(14) Zaera, F. Key Unanswered Questions about the Mechanism of Olefin Hydrogenation Catalysis by Transition-Metal Surfaces: A Surface-Science Perspective. *Phys. Chem. Chem. Phys.* **2013**, *15* (29), 11988−12003.

(15) Mattson, B.; Foster, W.; Greimann, J.; Hoette, T.; Le, N.; Mirich, A.; Wankum, S.; Cabri, A.; Reichenbacher, C.; Schwanke, E. Heterogeneous Catalysis: The Horiuti-Polanyi Mechanism and Alkene Hydrogenation. *J. Chem. Educ.* **2013**, *90* (5), 613−619.

(16) Farkas, A.; Farkas, L.; Rideal, E. K. Proc. R. Soc. A. *Experiments on Heavy Hydrogen IV - The Hydrogenation and Exchange Reaction of Ethylene with Heavy Hydrogen.* **1934**, *146* (858), 630−639.

(17) Ludwig, W.; Savara, A.; Dostert, K. H.; Schauermann, S. Olefin Hydrogenation on Pd Model Supported Catalysts: New Mechanistic Insights. *J. Catal.* **2011**, *284* (2), 148−156.

(18) Teschner, D.; Borsodi, J.; Wootsch, A.; Révay, Z.; Hävecker, M.; Knop-Gericke, A.; Jackson, S. D.; Schlögl, R. The Roles of Subsurface Carbon and Hydrogen in Palladium-Catalyzed Alkyne Hydrogenation. *Science (80-.).* **2008**, *320* (5872), 86−89.

(19) Mei, D.; Hansen, E. W.; Neurock, M. Ethylene Hydrogenation over Bimetallic Pd/Au(111) Surfaces: Application of Quantum Chemical Results and Dynamic Monte Carlo Simulation. *J. Phys. Chem. B* **2003**, *107* (3), 798−810.

(20) Yu, W. Y.; Mullen, G. M.; Mullins, C. B. Hydrogen Adsorption and Absorption with Pd-Au Bimetallic Surfaces. *J. Phys. Chem. C* **2013**, *117* (38), 19535−19543.

(21) van der Hoeven, J. E. S.; Ngan, H. T.; Taylor, A.; Eagan, N. M.; Aizenberg, J.; Sautet, P.; Madix, R. J.; Friend, C. M. Entropic Control of HD Exchange Rates over Dilute Pd-in-Au Alloy Nanoparticle Catalysts. *ACS Catal.* **2021**, *11* (12), 6971−6981.

(22) Han, J.; Mullins, C. B. Catalytic Reactions on Pd-Au Bimetallic Model Catalysts. *Acc. Chem. Res.* **2021**, *54* (2), 379−387.

(23) Shirman, E.; Shirman, T.; Shneidman, A. V.; Grinthal, A.; Phillips, K. R.; Whelan, H.; Bulger, E.; Abramovitch, M.; Patil, J.; Nevarez, R.; Aizenberg, J. Modular Design of Advanced Catalytic Materials Using Hybrid Organic-Inorganic Raspberry Particles. *Adv. Funct. Mater.* **2018**, *28* (27), 1704559.

(24) van der Hoeven, J. E. S.; Krämer, S.; Dussi, S.; Shirman, T.; Park, K. C. K.; Rycroft, C. H.; Bell, D. C.; Friend, C. M.; Aizenberg, J. On the Origin of Sinter-Resistance and Catalyst Accessibility in Raspberry-Colloid-Templated Catalyst Design. *Adv. Funct. Mater.* **2021**, *31*, 2106876.

(25) Shirman, T.; Toops, T. J.; Shirman, E.; Shneidman, A. V.; Liu, S.; Gurkin, K.; Alvarenga, J.; Lewandowski, M. P.; Aizenberg, M.; Aizenberg, J. Raspberry Colloid-Templated Approach for the Synthesis of Palladium-Based Oxidation Catalysts with Enhanced Hydrothermal Stability and Low-Temperature Activity. *Catal. Today* **2021**, *360* (March), 241−251.

(26) Luneau, M.; Guan, E.; Chen, W.; Foucher, A. C.; Marcella, N.; Shirman, T.; Verbart, D. M. A.; Aizenberg, J.; Aizenberg, M.; Stach, E. A.; Madix, R. J.; Frenkel, A. I.; Friend, C. M. Enhancing Catalytic Performance of Dilute Metal Alloy Nanomaterials. *Commun. Chem.* **2020**, *3* (1), 1−9.

(27) Luneau, M.; Shirman, T.; Filie, A.; Timoshenko, J.; Chen, W.; Trimpalis, A.; Flytzani-Stephanopoulos, M.; Kaxiras, E.; Frenkel, A. I.; Aizenberg, J.; Friend, C. M.; Madix, R. J. Dilute Pd/Au Alloy Nanoparticles Embedded in Colloid-Templated Porous SiO2: Stable Au-Based Oxidation Catalysts. *Chem. Mater.* **2019**, *31* (15), 5759−5768.

(28) Marcella, N.; Lim, J. S.; Płonka, A. M.; Yan, G.; Owen, C. J.; van der Hoeven, J. E. S.; Foucher, A. C.; Ngan, H. T.; Torrisi, S. B.; Marinkovic, N. S.; Stach, E. A.; Weaver, J. F.; Aizenberg, J.; Sautet, P.; Kozinsky, B.; Frenkel, A. I. Decoding Reactive Structures in Dilute Alloy Catalysts. *Nat. Commun.* **2022**, *13* (1), 1−9.

(29) Ngan, H. T.; Yan, G.; Hoeven, J. E. S. Van Der; Madix, R. J.; Cynthia, M. Hydrogen Dissociation Controls 1-Hexyne Selective Hydrogenation on Dilute Pd-in- Au Catalysts, **2022**, under review.

(30) Campbell, C. T. The Degree of Rate Control: A Powerful Tool for Catalysis Research. *ACS Catal.* **2017**, *7* (4), 2770−2779.

(31) O'Connor, C. R.; Duanmu, K.; Patel, D. A.; Muramoto, E.; van Spronsen, M. A.; Stacchiola, D.; Sykes, E. C.; Sautet, P.; Madix, R. J.; Friend, C. M. Facilitating Hydrogen Atom Migration via a Dense Phase on Palladium Islands to a Surrounding Silver Surface. *Proc. Natl. Acad. Sci. U. S. A.* **2020**, *117* (37), 22657−22664.

(32) Guan, E.; Foucher, A. C.; Marcella, N.; Shirman, T.; Luneau, M.; Head, A. R.; Verbart, D. M. A.; Aizenberg, J.; Friend, C. M.; Stacchiola, D.; Stach, E. A.; Frenkel, A. I. New Role of Pd Hydride as a Sensor of Surface Pd Distributions in Pd-Au Catalysts. *ChemCatChem* **2020**, *12* (3), 717−721.

(33) Tierney, H. L.; Baber, A. E.; Kitchin, J. R.; Sykes, E. C. H. Hydrogen Dissociation and Spillover on Individual Isolated Palladium Atoms. *Phys. Rev. Lett.* **2009**, *103* (24), 1−4.

(34) Lucci, F. R.; Darby, M. T.; Mattera, M. F. G.; Ivimey, C. J.; Therrien, A. J.; Michaelides, A.; Stamatakis, M.; Sykes, E. C. H. Controlling Hydrogen Activation, Spillover, and Desorption with Pd-Au Single-Atom Alloys. *J. Phys. Chem. Lett.* **2016**, *7* (3), 480−485.

(35) Brown, S. T.; Buitrago, P.; Hanna, E.; Scibek, R.; Nystrom, N. A. Bridges-2 : A Platform for Rapidly-Evolving and Data Intensive Research. *Pract. Exp. Adv. Res. Comput.* **2021**, 1−4.

(36) Towns, J.; Cockerill, T.; Dahan, M.; Gaither, K.; Grimshaw, A.; Hazlewood, V.; Lathrop, S.; Lifka, D.; Peterson, G. D. Scientific CyberinfraStructure XSEDE: Accelerating Scientific Discovery. *Comput. Sci. Eng.* **2014**, *16* (September/October), 62−74.

(37) Piella, J.; Bastús, N. G.; Puntes, V. Size-Controlled Synthesis of Sub-10-Nanometer Citrate-Stabilized Gold Nanoparticles and Related Optical Properties. *Chem. Mater.* **2016**, *28* (4), 1066−1075.

(38) Van Der Hoeven, J. E. S.; Deng, T. S.; Albrecht, W.; Olthof, L. A.; Van Huis, M. A.; De Jongh, P. E.; Van Blaaderen, A. Structural Control over Bimetallic Core-Shell Nanorods for Surface-Enhanced Raman Spectroscopy. *ACS Omega* **2021**, *6* (10), 7034−7046.

(39) Harrison, A. G.; Jones, E. G.; Gupta, S. K.; Nagy, G. P. Total Cross Sections for Ionization By Electron Impact. *Can. J. Chem.* **1966**, *44* (16), 1967−1973.

(40) Kresse, G.; Hafner, J. Ab Initio Molecular Dynamics for Liquid Metals. *Phys. Rev. B* **1993**, *47* (1), 558−561.

(41) Kresse, G.; Hafner, J. Ab Initio Molecular-Dynamics Simulation of the Liquid-Metalamorphous- Semiconductor Transition in Germanium. *Phys. Rev. B* **1994**, *49* (20), 14251−14269.

(42) Monkhorst, H. J.; Pack, J. D. Special Points for Brillouin-Zone Integrations. *Phys. Rev. B* **1976**, *13* (12), 5188−5192.

(43) Dion, M.; Rydberg, H.; Schröder, E.; Langreth, D. C.; Lundqvist, B. I. Van Der Waals Density Functional for General Geometries. *Phys. Rev. Lett.* **2004**, *92* (24), 22−25.

(44) Klimeš, J.; Bowler, D. R.; Michaelides, A. Chemical Accuracy for the van Der Waals Density Functional. *J. Phys.: Condens. Matter* **2010**, *22* (2), 022201.

(45) Román-Pérez, G.; Soler, J. M. Efficient Implementation of a van Der Waals Density Functional: Application to Double-Wall Carbon Nanotubes. *Phys. Rev. Lett.* **2009**, *103* (9), 096102.

(46) Henkelman, G.; Jónsson, H. A Dimer Method for Finding Saddle Points on High Dimensional Potential Surfaces Using Only First Derivatives. *J. Chem. Phys.* **1999**, *111* (15), 7010−7022.

(47) Momma, K.; Izumi, F. VESTA 3 for Three-Dimensional Visualization of Crystal, Volumetric and Morphology Data. *J. Appl. Crystallogr.* **2011**, *44* (6), 1272−1276.

(48) Gokhale, A. A.; Kandoi, S.; Greeley, J. P.; Mavrikakis, M.; Dumesic, J. A. Molecular-Level Descriptions of Surface Chemistry in Kinetic Models Using Density Functional Theory. *Chem. Eng. Sci.* **2004**, *59* (22−23), 4679−4691.

(49) Janthon, P.; Luo, S.; Kozlov, S. M.; Viñes, F.; Limtrakul, J.; Truhlar, D. G.; Illas, F. Bulk Properties of Transition Metals: A Challenge for the Design of Universal Density Functionals. *J. Chem. Theory Comput.* **2014**, *10* (9), 3832−3839.

(50) Cortright, R. D.; Dumesic, J. A. Kinetics of Heterogeneous Catalytic Reactions: Analysis of Reaction Schemes. *Adv. Catal.* **2001**, *46*, 161−264.

(51) Wang, T.; Ibañez, J.; Wang, K.; Fang, L.; Sabbe, M.; Michel, C.; Paul, S.; Pera-Titus, M.; Sautet, P. Rational Design of Selective Metal Catalysts for Alcohol Amination with Ammonia. *Nat. Catal.* **2019**, *2* (9), 773−779.